This is the peer-reviewed, final accepted version for American Mineralogist, published by the Mineralogical Society of America.
The published version is subject to change. Cite as Authors (Year) Title. American Mineralogist, in press.
DOI: https://doi.org/10.2138/am-2021-7714. http://www.minsocam.org/

Revision 1

Recycled volatiles determine fertility of porphyry deposits in collisional settings

Bo Xu[1,2], William L. Griffin[2], Zeng-Qian Hou[3], Yongjun Lu[4,5], Elena Belousova[2], Ji-Feng Xu[1] and Suzanne Y. O'Reilly[2],

[1]State Key Laboratory of Geological Processes and Mineral Resources, China University of Geosciences, Beijing 100083, China

[2]ARC Centre of Excellence for Core to Crust Fluid Systems (CCFS) and GEMOC, Macquarie University, NSW 2109, Australia

[3] Chinese Academy of Geological Sciences, Beijing 100037, China

[4] Geological Survey of Western Australia, 100 Plain Street, East Perth, WA 6004, Australia

[5] Centre for Exploration Targeting and CCFS, School of Earth Sciences, The University of Western Australia, Crawley, WA 6009, Australia

ABSTRACT

An intensive study of the geochemical characteristics (including the volatile elements Cl and S) of apatite associated with porphyry deposits was undertaken to address the debate about the crust- or mantle-derivation of their copper and gold, and to understand better, the controls on the transport of metals in magmatic fluids in

post-subduction settings. New geochemical data on apatite reveal parameters to discriminate mineralized porphyry systems across Iran, Tibet and western China from coeval barren localities across this post-subduction metallogenic belt. Apatites in *fertile* porphyries have higher Cl and S concentrations (reflecting water-rich crystallization conditions) than those from coeval *barren* ones. Our new isotopic data also indicate these volatiles are likely derived from pre-enriched sub-continental lithospheric mantle, metasomatized by previous oceanic subduction. This study demonstrates that refertilization of suprasubduction lithospheric mantle during previous collision events, is a prerequisite for forming post-subduction fertile porphyries, providing an evidence-based alternative to current ore-enrichment models.

INTRODUCTION

The Earth's mantle and crust contain little copper and gold and thus the concentration of these elements to form ore deposits requires explanation of their origin (crust or mantle) and the processes required (Sillitoe 2010). Volatiles such as chlorine, sulfur and water are of paramount importance for the transport and deposition of copper and gold (Griffin and O'Reilly 2013; Tassara et al. 2017), and carry the keys to examining this problem. The Tethyan metallogenic belt, extending from Europe through Iran to Tibet, is one of the world's major metal-producing belts. It contains many

post-collisional porphyry deposits, and is an ideal natural laboratory to examine the origins of important volatile components and the related mechanisms for post-subduction porphyry mineralisation.

Volatiles are difficult to study in whole-rock samples, owing to alteration and weathering. However, apatite concentrates volatiles (e.g. Cl and S), is ubiquitous in the lithospheric mantle (O'Reilly and Griffin 2000) and crust (Bruand et al. 2019) and especially crystallizes early in porphyry systems (Mao et al. 2016). It therefore can record a more complete history of evolution of volatiles in these magmas (Chelle-Michou et al. 2017).

In this study, we use *in situ* major- and trace-element geochemistry and Sr isotopes of magmatic apatite in porphyries from 12 porphyry Cu ± Au ± Mo deposits and 7 barren suites within the Tethyan metallogenic belt. The sample suite includes the largest porphyry deposits in each mineralised domain. These data reveal 1) anomalous enrichment of chlorine and sulfur in ore-forming magmas, and 2) a mantle isotopic signature in fertile suites.

SAMPLES

50 samples from 12 fertile porphyry deposits and 7 barren locations in four major post-subduction arcs (Fig. 1) have been analyzed, including the two largest porphyry systems in Iran, the Sarcheshmeh and Sungun deposits in the Kerman and Arasbaran

porphyry copper belt; the deposits in the Gangdese belt, southern Tibet; and the porphyry systems in the Sanjiang orogen in southeast Tibet (Fig. DR1). All samples represent post-collisional magmatism following cessation of active subduction. The description of the deposits and the barren plutons is given in the Data Repository. The apatite samples were collected from fresh magmatic apatite, without zoning and extensive resorption texture from BSE images (Data Repository). In order to yield robust apatite data, especially for the S, Cl and isotopic analysis, we carried out 244 major-, and 562 trace-elemental analysis on 7 different apatite standards and synthetic materials, including Durango (Mexico), Mad-blue, Mad-green (Madagascar), Moy (Myanmar), Mud Tank (Australia), Kovdor and Sly (Russia). Rb-Sr isotopes in apatites with different Sr concentrations were measured by the solution method and then used as monitoring standards. The description of standards and analytical methods is given in the Data Repository.

RESULTS

Chlorine, Sulfur and Rare-Earth Elements

The chlorine contents of apatite from the ore-forming porphyries are generally higher than those of apatite from the barren plutons (fertile suites: 0.08-0.34 wt%; median 0.13 wt%, average 0.17 wt%; barren suites: 0-0.34 wt%; median 0.03 wt%, average 0.04 wt%). For example, apatite in the Sarcheshmeh and Sungun porphyry Cu deposits contains 0.89

This is the peer-reviewed, final accepted version for American Mineralogist, published by the Mineralogical Society of America.
The published version is subject to change. Cite as Authors (Year) Title. American Mineralogist, in press.
DOI: https://doi.org/10.2138/am-2021-7714. http://www.minsocam.org/

to 1.36 wt % and 0.42 to 1.64 wt% Cl, respectively; comparative values are 0.12 to 0.58 wt% Cl in the Qulong porphyry Cu-Mo deposit, ~ 0.06 to 0.23 wt% Cl in the Jiama porphyry-skarn Cu-Mo-Au deposit, 0.02 to 0.12 wt% Cl in the Beiya porphyry-skarn Cu-Mo-Au deposit and 0.12 to 0.41 wt% Cl in the Machangqing porphyry deposit (Fig. 2A; Table1). In contrast, 95% apatites from barren suites contain less than 0.1 wt% Cl. Sulfur enters the apatite structure by complex substitutions including $Na^{+} + S^{6+} = Ca^{2+} + P^{5+}$ and $S^{6+} + Si^{4+} = 2P^{5+}$(Sha and Chappell 1999). The SO_3 contents in apatite from the fertile suites (< 0.96 wt%; median 0.15 wt%, average 0.19 wt%) are higher than those in apatite from the barren suites (< 0.75 wt%; median 0.07 wt%, average 0.10 wt%; Fig. 2A). REEs and Y are incorporated into the apatite structure via coupled substitution reactions (Hughes and Rakovan 2015): $Na^{+} + (Y+REE)^{3+} = 2\ Ca^{2+}$ and $Si^{4+} + (Y+REE)^{3+} = P^{5+} + Ca^{2+}$. Apatites in the mineralized samples have higher contents of REEs+Y (28-23000 ppm; median 520 ppm, average: 6650 ppm) than those in the barren rocks (68-55400 ppm; median 3230 ppm, average: 4110 ppm; Figs. 2B). The barren and fertile suites can also be distinguished on a series of trace-element plots involving $(Ce/Pb)_N$, $(La/Yb)_N$ and (V/Y) (Fig. 2B). In detail, apatites from most of the fertile-suite samples have higher $(La/Yb)_N$ (fertile suite: 2-206; median 67, average 73; barren suite: 0-155; median 18, average 23) and V/Y (fertile suite: < 0.4; median 0.04, average 0.05; barren suite: 0-18.0; median 0.02, average 0.17). The trace-element patterns of apatite from both

This is the peer-reviewed, final accepted version for American Mineralogist, published by the Mineralogical Society of America.
The published version is subject to change. Cite as Authors (Year) Title. American Mineralogist, in press.
DOI: https://doi.org/10.2138/am-2021-7714. http://www.minsocam.org/

95 groups display smooth patterns with relative enrichments of LREEs relative to HREEs.

96 All samples, except the Yao'an apatite, show negative Eu anomalies (Fig. DR4).

97 ***In situ* Sr- isotope compositions of apatite**

98 *In situ* Sr-isotope analyses (205 measurements) have been carried out on apatites from the

99 fertile rocks including Sungun, Sarcheshmeh, Masjed Daghi, Zhunuo, Jiama, Qulong,

100 Machangqing and Yaoan porphyres, and on apatite grains within the barren Zhada,

101 Nanmuqie, Renduoxiang, Wolong and Songgui plutons. Apatite in the fertile suites show

102 lower radiogenic $^{87}Sr/^{86}Sr_t$ (0.704-0.709, median 0.706, average 0.706), whereas apatite

103 from magmatic rocks of the barren suites has generally more radiogenic signatures

104 ($^{87}Sr/^{86}Sr_t$ = 0.705-0.712, median 0.708, average 0.708; Fig. 2D-2F).

105 **DISCUSSION**

106 **Apatite trace elements reveal the hydrous source of porphyry systems**

107 The euhedral apatites crystallized early, essentially coeval with, or before monazite and

108 xenotime (Suzuki et al 1992). Thus, euhedral apatite can be used as an indicator mineral

109 to trace the composition of its parental melts. The role of high contents of magmatic

110 water during the formation of porphyry-forming magmas has been widely discussed and

111 is recognized as a key factor in the fertility of porphyry systems (Loucks 2014; Chiaradia

112 2014). Apatite in ore-forming magma has high V/Y (Fig.2B). These higher V contents in

the host magma indicates elevated contents of dissolved H_2O in the melt, which cause amphibole to advance in the crystallization sequence rather than titanomagnetite. V^{4+} partitions more strongly into magnetite coefficient than into amphibole ($D_V^{magnetite/melt}$ >130; $D_V^{amphibole/melt}$: 6.34-10.64; La Tourrette et al. 1991; Nandedkar et al. 2016). Thus, at high contents of H_2O in the melt, amphibole will reach saturation before titanomagnetite, so that more V remains in the residual melt, while Y continues to be efficiently extracted from the melt into amphibole (the amphibole/melt partition coefficient for Y is around 2-6 in andesitic melts; Ewart and Griffin, 1994). Therefore, apatite trace-element proxies for amphibole in the differentiation series are especially useful indicators of the hydration state of the melt as well as the pressure at which differentiation took place (Loucks 2014; Davidson et al. 2007). This is consistent with the geochemistry of such magmas, which are characterized by small negative Eu anomalies and high V/Sc and Sr/Y (Loucks 2014), reflecting early amphibole fractionation and suppression of plagioclase crystallization in hydrous melts (Davidson et.al. 2007). Moreover, the rare-earth elements entrained by apatite are incompatible during magma evolution, and thus higher REEs in apatite also may suggest a hydrous magma. In detail, LREEs (e.g., La, Ce) are more compatible in hydrous melts than HREEs and Pb. As a consequence, hydrous melts usually contain higher LREE, which can be expressed by their $(Ce/Pb)_N$ ratio(Davidson et.al. 2007). It is thus expected that the apatite in hydrous magmas should have higher $(Ce/Pb)_N$ than those in the relatively dry suites. Therefore, on

This is the peer-reviewed, final accepted version for American Mineralogist, published by the Mineralogical Society of America.
The published version is subject to change. Cite as Authors (Year) Title. American Mineralogist, in press.
DOI: https://doi.org/10.2138/am-2021-7714. http://www.minsocam.org/

133 plots of V/Y *vs* REE+Y (Fig. 2B) and V/Y *vs* $(Ce/Pb)_N$ and V/Y *vs* REE+Y (Fig. DR3),
134 the fertile suites mostly have higher ratios than barren suites, suggesting early amphibole
135 fractionation in melts and reflecting the more hydrous nature of ore-forming magmas.

136 **Contrasting volatiles and Sr isotope compositions between fertile and barren melts**
137 **in post-subduction settings**

138 The composition of apatite can be used to calculate chlorine and sulfur
139 concentrations in the parental melt, provided that the apatite and melt were in equilibrium,
140 and that the experimental partition coefficients of these volatile components between the
141 apatite and concomitant melt are known. The experimental and analytical results indicate
142 that F, Cl and OH in apatite can diffuse relatively rapidly along the crystallographic
143 c-axis, and compositional gradients in these components can be observed if
144 post-magmatic changes in temperature, pressure, and fluid or melt composition have
145 occurred (Brenan 1993). Given these diffusion rates, the resistance of apatite to late
146 re-equilibration may only be satisfied when the system cools rapidly (1°C/ 100 years;
147 Brenan et al. 1995), conditions which are likely in eruptive magmas or very shallowly
148 emplaced melts (Piccoli and Candela 2002). However, these conditions may not easily be
149 reached in porphyry magmas. We have analyzed the apatites from core to rim by electron
150 microprobe analysis (EMPA), in order to quantify the degree of diffusion (Fig. DR3).
151 Cathodoluminescence and back-scattered electron images were used to select analytical

152 points. The Cl contents from core to rim show little sign of zoning, indicating our
153 samples were not affected by diffusion. Therefore, the chlorine contents of these apatites
154 can be used to calculate the chlorine concentrations of the coexisting melt. Several
155 previous experimental studies have determined the partitioning behavior of Cl and/or F in
156 the apatite-fluids-silicate melt system at different shallow-crustal conditions (Parat and
157 Holtz. 2005). We have used the recently calibrated apatite/melt chlorine partitioning
158 model of Li and Hermann (2017), based on experimental data from Webster et al. (2009)
159 at 200 MPa and 900 °C. We argue that the experimental conditions are reasonably close
160 to those inferred at the time of apatite crystallization and that the thermodynamic
161 parameters can be applied to determine the chlorine melt content in equilibrium with
162 apatite; the detailed function and results are given in the Data Repository. Using a set of
163 natural and experimental apatite/melt partitioning data for andesitic to rhyolitic melts,
164 Parat et al. (2011) calibrated the following empirical non-Henrian partitioning
165 relationship for sulfur between apatite and melt: $S_{apatite}(wt\%) = 0.0629 \times \ln S_{melt}(wt\%)$
166 + 0.4513.

167 The application of these calculations (Table 1) show that fertile suites have higher
168 Cl and S contents in the melt (Cl: 0-4.8 wt%; median 0.13 wt%, average 0.22 wt%; S:
169 8-3490 ppm; median 19 ppm, average 64 ppm), compared with barren suites (Cl: < 0.33
170 wt %, median 0.001 wt%, average 0.01 wt%; S: < 816 ppm, median 12 ppm, average 22
171 ppm). For example, the parental melt of the world-class Sarcheshmeh porphyry Cu

deposit contained up to 3.8 wt% Cl and 14-28 ppm S. Comparative values are 0 to 3.2 wt% Cl and 10-395 ppm S in the Qulong porphyry Cu-Mo deposit, 0.03 to 0.9 wt% Cl and 9-86 ppm S in the Jiama porphyry-skarn Cu-Mo-Au deposit, and 0-4.8wt% Cl and 15-827ppm S in the Machangqing porphyry deposit (Table 1). These results are also similar with subduction-related porphyries system, the Coroccohuayco Fe–Cu–Au porphyry–skarn deposit, Peru (Chelle-Michou and Chiaradia, 2017), and Red Chris porphyry Cu-Au deposit in British Columbia (Zhu et al. 2018). This is consistent with other suggestions that high Cl concentrations in the melts may be a prerequisite for the formation of porphyry-related ore deposits (Hsu et al., 2019), From fluid inclusion studies, the porphyry mineralization has shown that the hypersaline liquid and vapor are enriched in chlorine sulfur (Sillitoe, 2010), which are consistent with the elevated chlorine and sulfur in magmatic apatite of fertile porphyries. It is commonly accepted that chlorine and sulfur are of paramount importance for supporting the transport and deposition of ore metals at magmatic-hydrothermal systems. Specifically, chlorine and sulfur are critical elements of ore-forming fluids due to their capacity to form ligands with ore metals such as Cu, Au, Pb, Zn, Fe, Mo, as well as with other cations such as H^+, K^+, Na^+, Ca^+ which permit their transport to the site of ore deposition and cause hydrothermal alteration (e.g. Chelle-Michou and Chiaradia, 2017).

The $^{87}Sr/^{86}Sr$ ratio in apatite can record the initial Sr isotopic value of the magma, because Rb is highly incompatible in apatite ($D_{Rb}^{apatite/melt} = 0.0013$; Prowatke and

192 Klemme 2006). The $^{87}Sr/^{86}Sr$ ratio of apatite showing similar in these whole-rock
193 samples (e.g., Hou et al., 2015, Lu et al., 2015). The apatites in the fertile suites show a
194 mantle $^{87}Sr/^{86}Sr$ signature (0.704-0.706) and higher Cl/F, Cl and S in the melts compared
195 with barren plutons (Fig. 2D-2F), suggesting that the mantle source of the magmas also
196 supplied the volatiles necessary for mineralization. The mantle origin of apatite in the
197 fertile suites is further supported by apatite trace-element ratios (La/Sm and Th/U)
198 consistent with previous findings of host-rock petrogenesis worldwide (Belousova et al.
199 2002; Fig. 2D and 2E).

200 **The recycled mantle origins of volatiles in the post-subduction porphyry deposits**

201 The ore-forming magmas have higher Cl and S concentration with less radiogenic
202 $^{87}Sr/^{86}Sr$ (Fig. 2E and 2F). We therefore use these Sr isotope and Cl content modeled
203 mixing between altered ocean crust (AOC; mean $^{87}Sr/^{86}Sr$ 0.705; Sr 180 ppm; Staudigel
204 et al. 1995; Cl 2000 ppm; Kendrick et al. 2017), post-subduction lithospheric mantle
205 (PLM; Tibetan peridotite xenoliths with $^{87}Sr/^{86}Sr$, 0.714; Sr, 83.5 ppm(Xu et al. 2017); Cl:
206 200 ppm; and depleted MORB mantle (DMM; $^{87}Sr/^{86}Sr$, 0.7025; Sr, 15 ppm; Cl, 2 ppm;
207 John et al. 2010), to determine sources of these volatiles. In this modelling, the chlorine
208 from fertile porphyries requires almost 80% Cl contribution from AOC, with 10%
209 post-subduction lithospheric mantle and/or 10% depleted MORB mantle (Fig. 2E). In
210 contrast, apatite from barren suites inherits only 10-20% Cl from AOC (Fig. 2E). The

plot of $^{87}Sr/^{86}Sr$ *vs* apatite S (Fig. 2F) also shows a large contribution from both AOC and depleted MORB mantle. This modeling suggests that the higher Cl and S contents of fertile porphyries are consistent with derivation primarily from dehydration of altered oceanic basalts during subduction. This is consistent with the high chlorine concentration of serpentinized lithosphere (up to 2000 ppm Cl; Kendrick et al 2017) and the positive $\delta^{34}S$ compositions of arc magmas, consistent with those of seafloor sediments (de Hoog et al. 2001). Glass inclusions in olivine from primitive arc magmas have S concentrations up to 2900 ppm (de Hoog et al. 2001), and experimental A concentrations of oxidized arc basalts can be up to 1.5 wt.% S (Jugo et al. 2005). These high chlorine and sulfur contents have significance for the behavior of chalcophile and siderophile metals in genesis of porphyry Cu-Au deposit. The Cenozoic porphyry systems of Iran, Tibet and western China developed in post-subduction settings, when the AOC and DMM sources were no longer available. We thus propose that the higher chlorine and sulfur in post-subduction Cu-Au deposits were derived from the SCLM metasomatized by previous oceanic subduction (Fig. 3).

In this model, the dehydration of altered oceanic slab (200-65Ma; the period of during oceanic subduction) introduced a large amount of volatiles including Cl, S and water into the SCLM of the mantle wedge (stage A; Fig. 3A), resulting in the formation of volatile-rich reservoirs in the SCLM. These may be documented by the presence of

metasomatized phlogopite-bearing peridotite xenoliths entrained by Tibetan Miocene mantle-derived K-rich melts (phlogopite with 0.08 wt% Cl; Liu et al. 2011), hornblende- and phlogopite-bearing gabbro (Xu et al. 2019) in the Gangdese belts, and phlogopite- and apatite-bearing peridotites in NW Iran (Pang et al. 2013). During the continental collision that followed the subduction (stage B: ~15 Ma in Iran and Tibet; Fig. 3B), the existing volatile-bearing SCLM partially melted, with heat provided mainly by asthenospheric upwelling due to slab breakoff or the tearing or thinning of the passive continental lithospheric root (e.g., Xu et al. 2017), producing Cl- and S-enriched mantle-derived magmas (stage B; Fig. 3B). This generated widespread potassium-rich melts such as the Miocene Kerman, Miocene Gangdese and Yunnan Eocene lamprophyres (Xu et al 2017; Pang et al. 2013). These mafic melts underplated at the base of the crust, resulting in thermal and mass exchange during magma mixing and mingling with the overlying lower crust. This interaction led to the enrichment of volatiles in the lower crust, lowered melting temperatures to 700-750℃ (Lu et.al., 2015) and promoting melting of mafic lower crust, and generated the shoshonitic and high-K calc-alkaline ore-forming porphyries (Yang et al. 2015).

The high chlorine and sulfur contents of the magmas suppress the segregation of significant amounts of sulfide phases, leading to substantial metal enrichment in the evolving magma rather than in the cumulate rocks of the continental root. Thus, the

249 degree of metal enrichment in the post-subduction settings, and the generation of
250 world-class porphyry systems in such settings, depends on the availability of recycled
251 chlorine and sulfur. Refertilisation of the subcontinental lithospheric mantle by volatiles
252 derived from earlier subduction is a key factor in forming post-subduction porphyries;
253 this provides an alternative view to current ore enrichment models focusing on lower
254 crust melting.

255 **Implications for exploration: porphyry systems**

256 Relatively little geological work has been done in some areas of the Tethyan belt,
257 such as Iran, Pakistan, Afghanistan and even Tibet, and therefore the volatiles,
258 trace-element contents, and Sr isotopes of apatite could usefully fingerprint fertile
259 intrusions associated with mineralization. The robust trace-element ratios and Sr isotopes
260 of apatite can record more information especially of Cl and S evolution, which are key to
261 the genesis of porphyry systems. Analyzing the compositions of apatite from an area with
262 little geologic information or poor outcrop could efficiently and cheaply discriminate
263 whether the drainage source area is dominated by unprospective crustally-derived
264 granitoids or by prospective mantle-associated granitoids. This could help to focus
265 exploration on the most prospective areas.

266 Large porphyry ore deposits can be formed by combinations of "common"
267 geological processes, but all of these processes must be optimized to form a giant deposit.

The data presented here suggest that higher volatile contents are advantageous for forming large porphyry deposits because of the optimization of ore-metal transport in such chlorine- and sulfur-rich fluids

CONCLUSIONS

Robust trace-element and Sr isotope data on apatite can distinguish fertile (porphyry Cu ± Au) magmas from barren magmatic suites. The fertility indicators are Cl/F (>0.19), V/Y (>0.008) and $(Ce/Pb)_N$ ratios (>2138), which are higher than in apatite from the barren suites; these elevated ratios reflect a volatile-enriched magma. Their less radiogenic Sr isotopes indicate that the higher volatile contents advantageous for ore-metal transport such chlorine- and sulfur-rich fluids reflect the derivation from the previously metasomatized mantle. This observation indicates the importance of volatiles, recycled from previous oceanic subduction, in collisional settings.

Acknowledgments

REFERENCES CITED

Belousova E A, Griffin W L, O'Reilly S Y, et al. (2002) Apatite as an indicator mineral for mineral exploration: trace-element compositions and their relationship to host rock type. Journal of Geochemical Exploration, 76(1), 45-69.

285 Brenan, J. (1993) Kinetics of fluorine, chlorine and hydroxyl exchange in fluorapatite.
286 Chemical Geology, 110(1-3), 195-210.

287 Brenan J M, Shaw H F, Ryerson F J, et al. (1995) Mineral-aqueous fluid partitioning of
288 trace elements at 900 C and 2.0 GPa: Constraints on the trace element chemistry of
289 mantle and deep crustal fluids. Geochimica et Cosmochimica Acta, 59(16),
290 3331-3350.

291 Bruand, E., Storey, C., Fowler, M., and Heilimo, E. (2019) Oxygen isotopes in titanite
292 and apatite, and their potential for crustal evolution research. Geochimica et
293 Cosmochimica Acta, 255, 144-162.

294 Chelle-Michou, C., and Chiaradia, M. (2017) Amphibole and apatite insights into the
295 evolution and mass balance of Cl and S in magmas associated with porphyry copper
296 deposits. Contributions to Mineralogy and Petrology, 172(11-12), 105.

297 Chiaradia, M. (2014) Copper enrichment in arc magmas controlled by overriding plate
298 thickness. Nature Geoscience, 7(1), 43.

299 Davidson J, Turner S, Handley H, et al. (2007) Amphibole “sponge” in arc crust?
300 Geology, 35(9), 787-790.

de Hoog, J.C.M., Mason, P.R.D., and van Bergen, M.J., (2001) Sulfur and chalcophile elements in subduction zones: Constraints from a laser ablation ICP-MS study of melt inclusions from Galunggung Volcano, Indonesia. Geochimica et Cosmochimica Acta, 65, 3147–3164.

Ewart A, Griffin W L. (1994) Application of proton-microprobe data to trace-element partitioning in volcanic rocks. Chemical Geology, 117(1-4), 251-284.

Griffin, W. L., Begg, G. C., and O'Reilly, S. Y. (2013) Continental-root control on the genesis of magmatic ore deposits. Nature Geoscience, 6(11), 905.

Hou, Z., Yang, Z., Lu, Y., Kemp, A., Zheng, Y., Li, Q., ... & Duan, L. (2015). A genetic linkage between subduction-and collision-related porphyry Cu deposits in continental collision zones. Geology, 43(3), 247-250.

Hsu, Y-J, Zajacz, Z., Ulmer, P., and Heinrich, C.A., (2019) Chlorine partitioning between granitic melt and H2O-CO2-NaCl fluids in the Earth's upper crust and implications for magmatic-hydrothermal ore genesis: Geochimica et Cosmochimica Acta, 261, 171-190.

Hughes J M, and Rakovan J F. (2015) Structurally robust, chemically diverse: apatite and apatite supergroup minerals. Elements, 11(3), 165-170.

John, T., Layne, G. D., Haase, K. M., and Barnes, J. D. (2010) Chlorine isotope evidence for crustal recycling into the Earth's mantle. Earth and Planetary Science Letters, 298(1-2), 175-182.

Jugo, P. J., Luth, R. W., and Richards, J. P. (2005) Experimental data on the speciation of sulfur as a function of oxygen fugacity in basaltic melts. Geochimica et Cosmochimica Acta, 69(2), 497-503.

Kendrick M A, Hémond C, Kamenetsky V S, et al. (2017) Seawater cycled throughout Earth's mantle in partially serpentinized lithosphere. Nature geoscience, 10(3), 222.

La Tourrette T Z, Burnett D S, and Bacon C R. (1991) Uranium and minor-element partitioning in Fe-Ti oxides and zircon from partially melted granodiorite, Crater Lake, Oregon. Geochimica et Cosmochimica Acta, 55(2), 457-469.

Li and Hermann (2017), The effect of fluorine and chlorine on trace element partitioning between apatite and sediment melt at subduction zone conditions. Chemical geology, 473, 55-73.

Liu, C. Z., Wu, F. Y., Chung, S. L., and Zhao, Z. D. (2011). Fragments of hot and metasomatized mantle lithosphere in Middle Miocene ultrapotassic lavas, southern Tibet. Geology, 39(10), 923-926.

335 Loucks R R. (2014) Distinctive composition of copper-ore-forming arcmagmas.
336 Australian Journal of Earth Sciences, 61(1): 5-16.

337 Lu, Y.J., Loucks, R.R., Fiorentini, M.L., Yang, Z.M., and Hou, Z.Q. (2015) Fluid flux
338 melting generated post-collisional high-Sr/Y copper-ore-forming water-rich magmas
339 in Tibet: Geology, 43, 583–586.

340 Mao, M., Rukhlov, A. S., Rowins, S. M., Spence, J., and Coogan, L. A. (2016) Apatite
341 trace element compositions: A robust new tool for mineral exploration. Economic
342 Geology, 111(5), 1187-1222.

343 Nandedkar, R. H., Hürlimann, N., Ulmer, P., and Müntener, O. (2016) Amphibole–melt
344 trace element partitioning of fractionating calc-alkaline magmas in the lower crust:
345 an experimental study. Contributions to Mineralogy and Petrology, 171(8-9), 71.

346 O'Reilly, S. Y., and Griffin, W. L. (2000) Apatite in the mantle: implications for
347 metasomatic processes and high heat production in Phanerozoic mantle. Lithos,
348 53(3-4), 217-232.

349 Pang, K. N., Chung, S. L., Zarrinkoub, M. H., Lin, Y. C., Lee, H. Y., Lo, C. H., and
350 Khatib, M. M. (2013) Iranian ultrapotassic volcanism at~ 11 Ma signifies the
351 initiation of post‐collisional magmatism in the Arabia-Eurasia collision zone. Terra
352 Nova, 25(5), 405-413.

353 Parat F, Holtz F. (2005) Sulfur partition coefficient between apatite and rhyolite: the role
354 of bulk S content. Contributions to Mineralogy and Petrology, 150(6), 643-651.

355 Parat, F., Holtz, F., and Klügel, A. (2011) S-rich apatite-hosted glass inclusions in
356 xenoliths from La Palma: constraints on the volatile partitioning in evolved alkaline
357 magmas. Contributions to Mineralogy and Petrology, 162(3), 463-478.

358 Piccoli P M, and Candela P A. (2002) Apatite in igneous systems. Reviews in
359 Mineralogy and Geochemistry, 48(1), 255-292.

360 Prowatke, S., and Klemme, S. (2006) Trace element partitioning between apatite and
361 silicate melts. Geochimica et Cosmochimica Acta, 70(17), 4513-4527.

362 Sha L K, and Chappell B W. (1999) Apatite chemical composition, determined by
363 electron microprobe and laser-ablation inductively coupled plasma mass
364 spectrometry, as a probe into granite petrogenesis. Geochimica et Cosmochimica
365 Acta, 63(22): 3861-3881.

366 Sillitoe, R.H. (2010) Porphyry copper systems. Econ. Geol, 105, 3–41.

367 Staudigel, H., Davies, G. R., Hart, S. R., Marchant, K. M., and Smith, B. M. (1995) Large
368 scale isotopic Sr, Nd and O isotopic anatomy of altered oceanic crust: DSDP/ODP
369 sites417/418. Earth and Planetary Science Letters, 130(1-4), 169-185.

370 Suzuki, Kazuhiro, et al. (1992) Intra-grain distribution of REE and crystallization
371 sequence of accessory minerals in the Cretaceous Busetsu Granite at Okazaki,
372 central Japan. Geochemical Journal, 26.6, 383-394.

373 Tassara, S., González-Jiménez, J. M., Reich, M., Schilling, M. E., Morata, D., Begg, G.
374 and Barra, F. (2017) Plume-subduction interaction forms large auriferous provinces.
375 Nature communications, 8(1), 843.

376 Webster J D, Tappen C M, and Mandeville C W. (2009) Partitioning behavior of chlorine
377 and fluorine in the system apatite–melt–fluid. II: Felsic silicate systems at 200 MPa.
378 Geochimica et Cosmochimica Acta, 73(3), 559-581.

379 Xu, B., Griffin, W. L., Xiong, Q., Hou, Z. Q., O'Reilly, S. Y., Guo, Z., and Zheng, Y. C.
380 (2017) Ultrapotassic rocks and xenoliths from South Tibet: Contrasting styles of
381 interaction between lithospheric mantle and asthenosphere during continental
382 collision. Geology, 45(1), 51-54.

383 Xu, W., Zhu, D. C., Wang, Q., Weinberg, R. F., Wang, R., Li, S. M., and Zhao, Z. D.
384 (2019) Constructing the Early Mesozoic Gangdese Crust in Southern Tibet by
385 Hornblende-dominated Magmatic Differentiation. Journal of Petrology, 60(3),
386 515-552.

Yang, Z. M., Lu, Y. J., Hou, Z. Q., and Chang, Z. S. (2015). High-Mg diorite from Qulong in southern Tibet: Implications for the genesis of adakite-like intrusions and associated porphyry Cu deposits in collisional orogens. Journal of Petrology, 56(2), 227-254.

Zhu, J. J., Richards, J. P., Rees, C., Creaser, R., and Jürgen Lang. (2018). Elevated magmatic sulfur and chlorine contents in ore-forming magmas at the red chris porphyry Cu-Au deposit, northern British Columbia, Canada: Economic Geology, v. 113, p.1047-1075.

FIGURE CAPTIONS

Figure 1. Global relief map showing the distribution of the fertile and barren magmatic suites investigated in this study (listed in Table 1). The names of the fertile and barren suites used in this study are labeled in the map.

Figure 2. (A) Apatite Cl (wt%) vs SO_3 (wt%), (B) Apatite REE+Y (ppm) vs V/Y plot, (C) Apatite Th/U vs La/Sm, (D) Apatite Cl/F vs $^{87}Sr/^{86}Sr$ plot, (E) Apatite chlorine in melts vs $^{87}Sr/^{86}Sr$ plot, (F) Apatite sulfur in melts vs $^{87}Sr/^{86}Sr$ plot, showing that most fertile suites have high Cl, REE+Y content, and V/Y ratio; the fertile porphyries also have high chlorine and sulfur content in melts with less radiogenic $^{87}Sr/^{86}Sr$.

Figure 3. Evolution of volatiles in post-subduction setting.

405 (A) Stage A: during oceanic slab subduction, dehydration of the subducting oceanic crust
406 leads to partial melting of asthenosphere. Volatile-enriched basaltic melts intrude the
407 overlying lithosphere and enrich Cl, S and water at continental root, generate
408 metasomatized phlogopite-bearing SCLM.

409 (B) Stage B: during continental collision period, upwelling of asthenospheric mantle
410 triggers remelting of previous metasomatised volatile-enriched SCLM, introduced melts
411 capable of scavenging chlorine and sulfur from formerly enriched lithosphere root.
412 Underplate of these Cl- and S-rich mafic magma mixing and mingling with the overlying
413 lower crust, leading to formation of fertile magmas for post-collisional porphyry systems.

414 Table 1. The composition of Cl and SO_3 in apatites, and calculated melt chlorine and
415 sulfur concentration (ppm) from Barren and Fertile Magmatic Suites. Calculated melt
416 chlorine according to Li and Hermann (2017) and melt sulfur composition using the
417 apatite-melt partition coefficient formula of Parat et al (2011).

418

419

This is the peer-reviewed, final accepted version for American Mineralogist, published by the Mineralogical Society of America.
The published version is subject to change. Cite as Authors (Year) Title. American Mineralogist, in press.
DOI: https://doi.org/10.2138/am-2021-7714. http://www.minsocam.org/

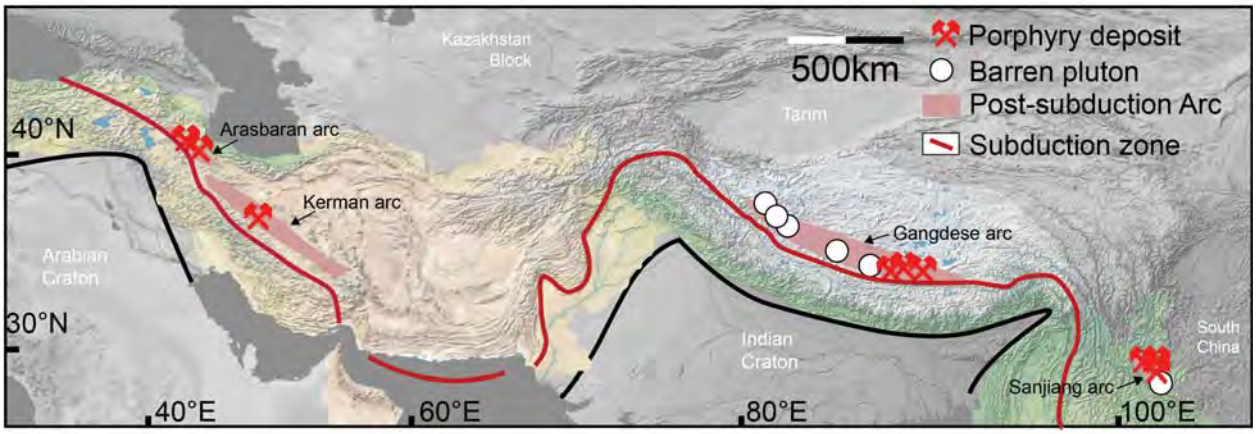

Figure1

This is the peer-reviewed, final accepted version for American Mineralogist, published by the Mineralogical Society of America.
The published version is subject to change. Cite as Authors (Year) Title. American Mineralogist, in press.
DOI: https://doi.org/10.2138/am-2021-7714. http://www.minsocam.org/

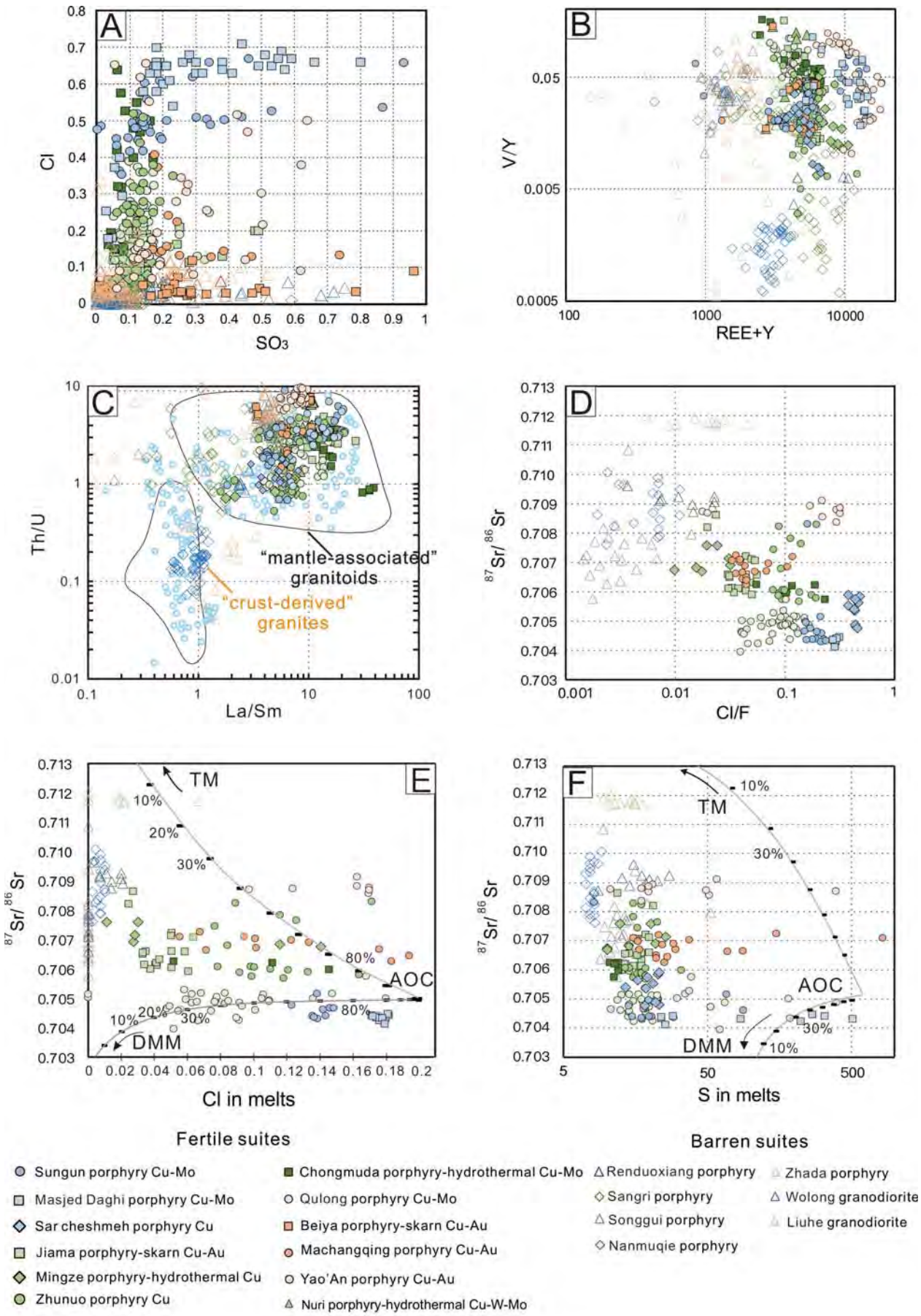

Figure 2

This is the peer-reviewed, final accepted version for American Mineralogist, published by the Mineralogical Society of America.
The published version is subject to change. Cite as Authors (Year) Title. American Mineralogist, in press.
DOI: https://doi.org/10.2138/am-2021-7714. http://www.minsocam.org/

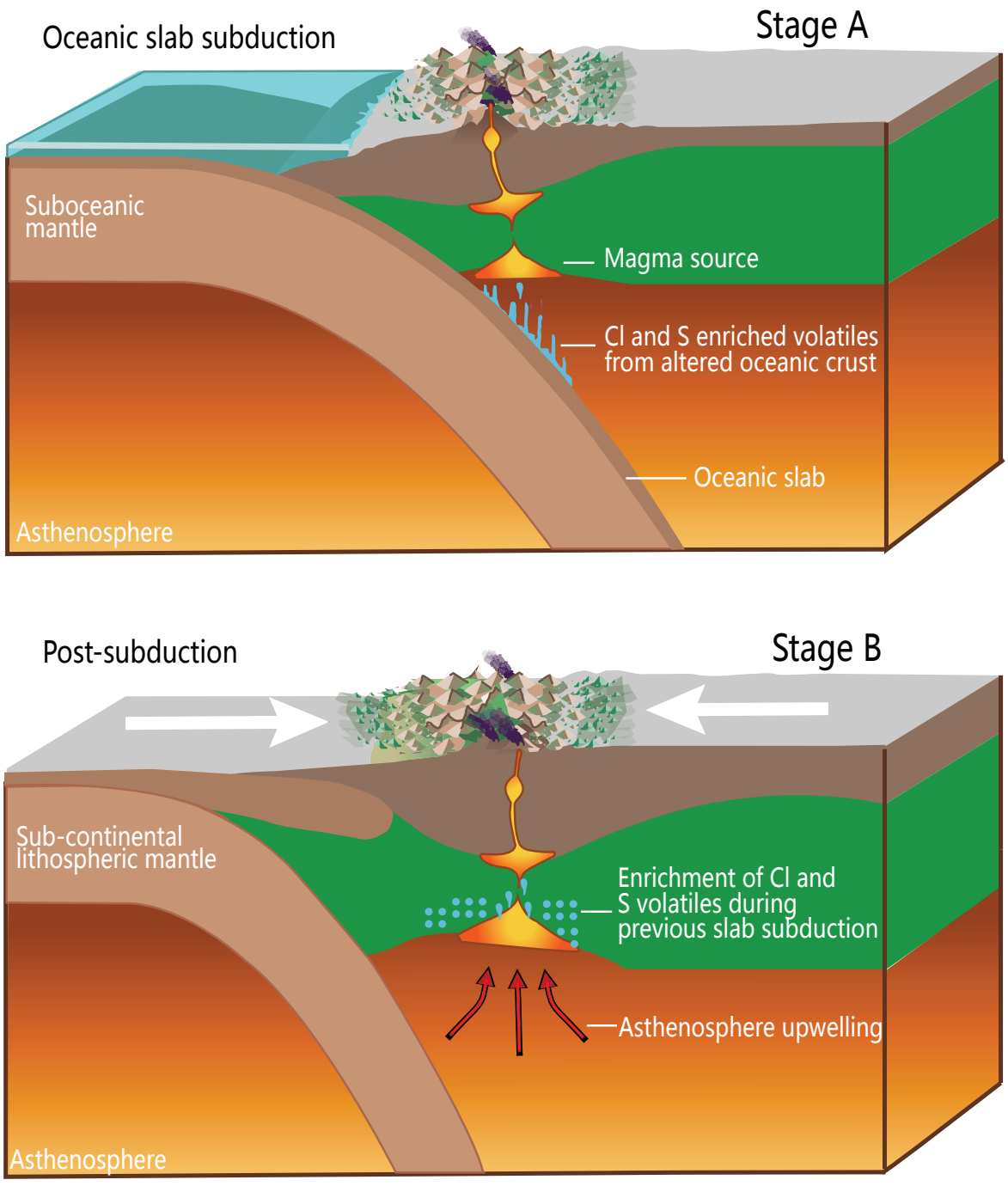

Figure 3

This is the peer-reviewed, final accepted version for American Mineralogist, published by the Mineralogical Society of America.
The published version is subject to change. Cite as Authors (Year) Title. American Mineralogist, in press.
DOI: https://doi.org/10.2138/am-2021-7714. http://www.minsocam.org/

Table 1 Infertile and Fertile Magmatic Suites Used in This Work

Sample	Deposit type	Apatite Cl (wt%)				Cl in melts (ppm)				Apatite SO_3(wt%)				S in melts (ppm)			
		Max	Min	Ave	Med	Max	Min	Ave	Med	Max	Min	Ave	Med	Max	Min	Ave	Med
Masjed Daghi	Cu-Au	1.91	0.18	1.28	1.83	16529	1462	2695	1774	0.24	0.03	0.13	0.15	509.88	9.05	74.22	26.63
Sungun	Cu-Au	1.64	0.42	1.02	1.02	4475	1122	2400	2248	0.93	0.10	0.22	0.16	254.66	7.62	34.51	21.17
Sarcheshmeh	Cu-Au	1.36	0.89	1.17	1.18	382127	3825	32472	5424	0.20	0.09	0.15	0.16	27.93	13.51	20.52	20.64
Qulong	Cu-Mo	0.58	0.12	0.25	0.23	120095	474	4341	903	0.62	0.05	0.16	0.14	395.20	7.62	32.68	17.60
Zhunuo	Cu-Mo	0.52	0.22	0.29	0.27	1712	766	1025	972	0.23	0.06	0.12	0.12	32.96	11.16	17.13	15.85
Jiama	Cu-Au	0.23	0.06	0.14	0.14	8715	246	746	565	0.49	0.03	0.13	0.12	85.69	9.46	17.48	16.36
Chongmuda	Cu-Mo	0.64	0.14	0.38	0.40	3090	488	1264	1193	0.17	0.03	0.10	0.09	22.49	9.46	13.73	12.68
Nuri	Au-Cu	0.20	0.07	0.96	0.08	2169	0	347	0	0.28	0.12	0.22	0.23	45.61	16.46	32.91	32.03
Beiya	Au-Cu	0.12	0.02	0.04	0.04	920	356	653	653	0.96	0.01	0.30	0.26	197.38	7.91	52.68	36.27
Machangqing	Cu-Au	0.41	0.12	0.18	0.15	48098	0	5420	1015	0.74	0.01	0.25	0.19	151.05	15.35	38.18	25.22
Yaoan	Au	0.70	0.04	0.29	0.16	54810	206	4359	1625	0.64	0.05	0.22	0.16	443.21	10.68	54.88	20.84
Mingze	Au	0.12	0.03	0.08	0.07	3493	12	1003	302	0.19	0.04	0.10	0.08	25.55	7.62	12.99	11.80
Zhada	Barren	0.20	0.02	0.12	0.13	673	0	383	425	0.44	0.00	0.12	0.11	125.58	7.62	20.42	15.64
Renduoxiang	Barren	0.08	0.00	0.03	0.03	766	0	101	85	0.24	0.00	0.08	0.08	35.35	7.62	14.10	12.36
Nanmuqie	Barren	1.27	0.00	0.05	0.02	3329	7	142	72	0.14	0.00	0.01	0.01	18.58	7.15	8.49	8.12
Sangri	Barren	0.40	0.00	0.03	0.03	1127	0	103	104	0.59	0.00	0.08	0.09	27.23	7.62	13.21	13.51
Wolong	Barren	0.06	0.00	0.01	0.01	0	0	0	0	0.72	0.00	0.15	0.05	742.46	7.62	73.87	10.54
Liuhe	Barren	0.34	0.00	0.06	0.04	1309	187	565	389	0.52	0.00	0.09	0.05	203.77	7.62	19.66	10.47
Songgui	Barren	0.06	0.00	0.02	0.01	0	0	0	0	0.75	0.02	0.14	0.09	210.36	8.38	25.73	12.84